Numerical simulations of residual stress formation and its effect on fatigue crack propagation in a fillet welded T-joint

Malschaert, David; Veljkovic, Milan; Maljaars, Johan

DOI
10.1016/j.engfracmech.2024.110236

Publication date
2024

Document Version
Final published version

Published in
Engineering Fracture Mechanics

Citation (APA)
Malschaert, D., Veljkovic, M., & Maljaars, J. (2024). Numerical simulations of residual stress formation and its effect on fatigue crack propagation in a fillet welded T-joint. *Engineering Fracture Mechanics*, *306*, Article 110236. https://doi.org/10.1016/j.engfracmech.2024.110236

Engineering Fracture Mechanics 306 (2024) 110236

Contents lists available at ScienceDirect

Engineering Fracture Mechanics

journal homepage: www.elsevier.com/locate/engfracmech

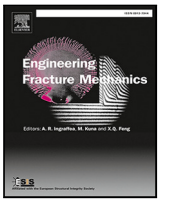

Numerical simulations of residual stress formation and its effect on fatigue crack propagation in a fillet welded T-joint

David Malschaert [a,*], Milan Veljkovic [a], Johan Maljaars [b,c]

[a] Department of Engineering Structures, Delft University of Technology, Stevinweg 1, Delft, 2628 CN, The Netherlands
[b] Department of Reliable Structures, TNO, Molengraaffsingel 8, Delft, 2629 JD, The Netherlands
[c] Department of the Built Environment, Eindhoven University of Technology, Het Kranenveld 8, Eindhoven, 5612 AZ, The Netherlands

ARTICLE INFO

Keywords:
T-joint
Residual stress
Welding simulation
Fatigue crack propagation
Fracture mechanics
LEFM
XFEM

ABSTRACT

The welding process induces residual stresses because of the non-uniform heating and cooling of the material. Residual stresses are known to influence fatigue crack growth. However, studies addressing both the formation of residual stress – giving a realistic multi-directional stress and strain field – and redistribution of residual stresses due to crack growth in the case of a surface crack have not been found. The extended finite element method was employed in this study to evaluate the stress intensity factors of a planar, growing crack in a welded T-joint with and without welding induced residual stresses. The initial residual stress field was taken from a welding simulation using the finite element method. The redistribution of the residual stress field due to crack growth was studied in addition to the shape and growth rate of the planar crack. The study shows that, in agreement with experimental evidence, the external stress ratio has a significant influence in the absence of residual stress but it does not have a significant influence in the presence of residual stress. The current study gives insight into the cause of this observation.

1. Introduction

Many steel structures are subjected to cyclic loading, which can result in fatigue crack initiation and growth. These cracks often originate from welded connections at stress concentration sites [1,2]. The welding process causes the formation of residual stresses, which influence the crack initiation and propagation [3–7]. These residual stresses develop during the non-uniform heating and cooling of the weld and adjacent material, affecting the mean stress during cyclic loading [8]. While methods exist for relieving [9] or modifying [10] residual stresses, implementing these approaches adds to overall manufacturing costs and may be impractical for large components. Under certain conditions, predicting the fatigue life of a specific joint can be improved by simulating fatigue crack growth in a residual stress field obtained through simulating the welding process [3,6,11].

T-joints are used to connect two steel plates in perpendicular planes. In the case of a T-joint, the residual stresses along the weld toe show a certain hat-shape curve for both the longitudinal (parallel to the weld) and transverse (perpendicular to the weld) directions, with the region halfway the length in tension [5,6,12,13]. A high local stress ratio is generally detrimental for fatigue [14]. Therefore, even if the external cyclic loading is in compression, the combined effect of cyclic loading and transverse residual stresses may induce tension, which enhances the nucleation and propagation of fatigue cracks. Various researchers have simulated fatigue crack propagation in T-joints under the influence of residual stresses [3–6]. Residual stresses in the vicinity of the crack tend to redistribute as the crack propagates [4,5,11,15]. The redistribution of the welding-induced residual stresses due

* Corresponding author.
E-mail address: D.H.Malschaert@tudelft.nl (D. Malschaert).

https://doi.org/10.1016/j.engfracmech.2024.110236
Received 12 March 2024; Received in revised form 4 June 2024; Accepted 9 June 2024
Available online 11 June 2024

Nomenclature

Latin symbols

$\frac{da}{dn}$	Crack propagation rate
a	Crack depth
b	Half width of the double ellipsoid heat source
C	Empirical constant of Paris equation
c	Half crack length
c_1	Front length of the double ellipsoid heat source
c_2	Rear length of the double ellipsoid heat source
d	Depth of the double ellipsoid heat source
f_1	Heat deposition fraction of the front part of the heat source
f_2	Heat deposition fraction of the rear part of the heat source
H	Stiffener height
H_W	Weld height
I	Amperage
K	Stress intensity factor
K_{max}	Maximum stress intensity factor
K_{min}	Minimum stress intensity factor
$K_{RS+L_{max}}$	Stress intensity resulting from the residual stress and the maximum value of the external loading
$K_{RS+L_{min}}$	Stress intensity resulting from the residual stress and the minimum value of the external loading
L	Specimen length
m	Empirical constant of Paris equation
Q	Power input
q_f	Power density distribution at the front of the heat source
q_r	Power density distribution at the rear of the heat source
R	Externally applied stress ratio
r_y	Radius of the plastic zone at the crack front
R_{eff}	Effective stress intensity factor ratio
T	Temperature
T_B	Base plate thickness
T_S	Stiffener thickness
U	Voltage
v	Welding speed
W	Base plate width
W_W	Weld width
$X_{L,c}$	Local X-coordinate of the crack
$X_{L,h}$	Local X-coordinate of the heat source
$Y_{L,h}$	Local Y-coordinate of the heat source
$Z_{L,c}$	Local Z-coordinate of the crack
$Z_{L,h}$	Local Z-coordinate of the heat source

Greek symbols

$\Delta\sigma$	Stress range
ΔK	Stress intensity factor range
ΔK_I	Mode I stress intensity factor range
ΔK_{II}	Mode II stress intensity factor range
ΔK_{III}	Mode III stress intensity factor range
Δn	Change in number of loading cycles
η	Welding efficiency
γ	Empirical constant of Walker equation
σ_{max}	Maximum applied stress
σ_{min}	Minimum applied stress
σ_{xx}	Nominal stress in X-direction
σ_{yy}	Nominal stress in Y-direction
θ	Projected ellipsoidal angle

Acronyms

BP	Base plate
FEM	Finite element method
LEFM	Linear elastic fracture mechanics
MAG	Metal active gas
RS	Residual stress
WFM	Weight function method
XFEM	Extended finite element method

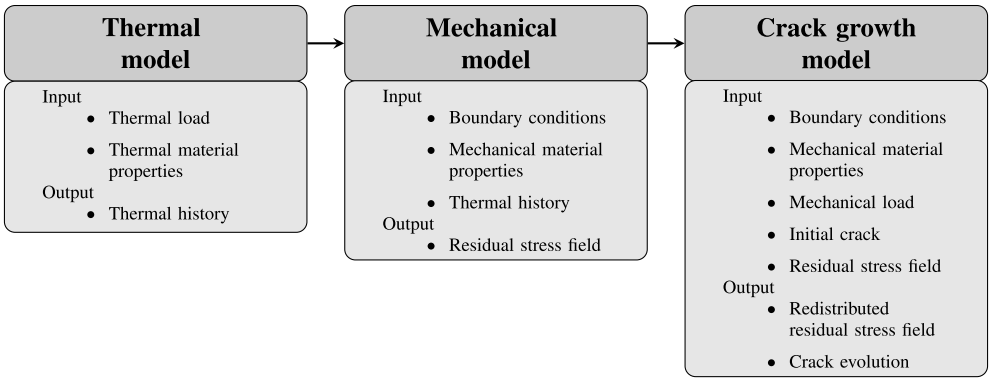

Fig. 1. Modelling approach.

to crack growth has been studied experimentally and numerically by Liljedahl et al. [16,17] for a through-thickness crack. The results showed an increase in residual stresses at the crack front as the crack grows compared to the residual stress field of the uncracked body. However, studies addressing both the formation of residual stress – giving a realistic multi-directional stress and strain field – and redistribution of residual stresses due to crack growth in the case of a surface crack have not been found. This paper describes a finite element simulation of a welding process aimed at predicting the welding-induced residual stresses in a fillet-welded T-joint. The current model represents a detail of a welded attachment oriented perpendicular to the main loading directions, which is often applied in bridges. The T-joint geometry (length, base plate thickness, and base plate width) have been varied to study their influence on residual stresses. Verification and validation of the finite element model of the welding process was conducted by comparing residual stresses with finite element results and experimental measurements, respectively, from various studies [18–22]. Subsequently, stepwise crack propagation due to an external cyclic load was simulated using XFEM in Abaqus/CAE 2022 in which residual stresses were included. The influence of residual stresses on crack growth was studied and the redistribution of these residual stresses due to crack growth are presented.

2. Methods and models

Fig. 1 illustrates the modelling approach, depicting the input and output utilised for each model. The welding procedure was modelled using a sequential thermal–mechanical analysis in Abaqus/CAE 2022. The thermal model included the thermal history where the heat, generated by the welding process, was simulated and distributed through the structure by conduction and dissipated to the surroundings through radiation and convection. This thermal history was imported into the physically non-linear mechanical model to obtain deformations and residual stresses. These residual stresses were subsequently applied as an initial condition in the physically non-linear XFEM model, where a small initial crack was inserted and subjected to cyclic loading to assess crack growth and the redistribution of residual stresses. Further elaboration will be provided in Sections 2.1, 2.2 and 2.3.

2.1. General model description

The T-joint consists of a stiffener and a base plate made of S355, welded together by two single-pass fillet welds. The welding passes were applied in reversed direction, as indicated in Fig. 2. A gap of 0.5 mm between the stiffener and the base plate was incorporated into the model to account for fabrication tolerances and to ensure that the stiffener and base plate were only connected through the welds. The model of the T-joint is depicted in Fig. 3. The coordinate system's origin was located on the top surface of the base plate, halfway between the width and length of the specimen. The X-axis was aligned with the specimen's length, the Y-axis with its width and the Z-axis with its height. The remainder of the dimensions of the models as well as the boundary conditions are discussed in Section 3.

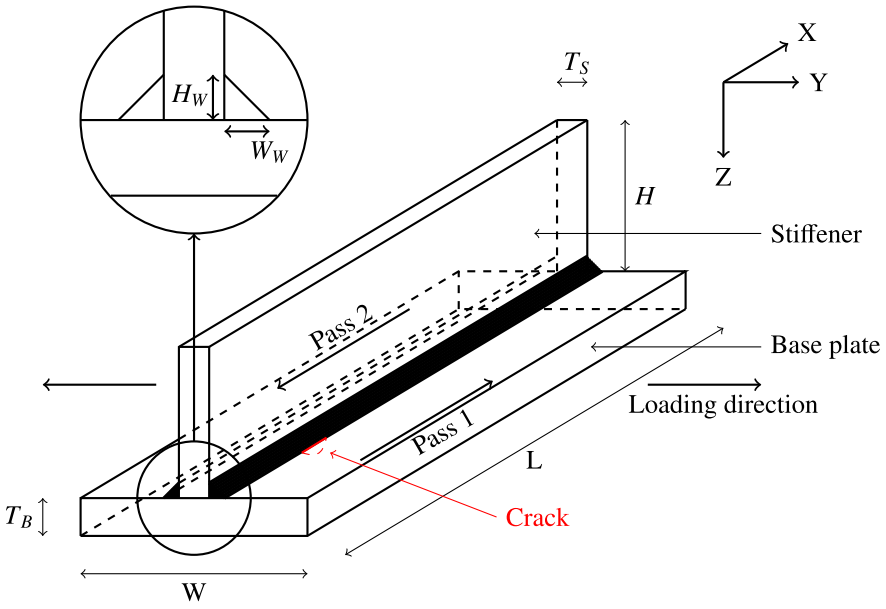

Fig. 2. T-joint geometry.

An element nodal distance of 2.5 mm and 5 mm were used for the weld region and the region outside the weld, respectively, in both the thermal and mechanical models. A refined mesh with an element nodal distance of 1.25 mm was used for the thermal model and mechanical model in the region around the welds. The element nodal distance outside this region was 5 mm (see Fig. 3(a)). The residual stress field from the mechanical model was mapped on the more refined mesh in the crack growth model, containing the uncracked body, with an element nodal distance of 0.2 mm (see Fig. 3(b)). The residual stresses where compared before and after mapping to ensure the mapping did not introduce any deviations in the residual stresses. Tie constraints were applied between regions with different meshes to ensure compatibility of temperature and displacement fields at the boundaries. Linear volume elements with full integration were used for the models using type DC3D8 for the thermal model and type C3D8 for the mechanical model. Enriched linear volume elements with full integration of type DC3D8 were used for the crack growth model. Fig. 3(c) presents the cracked elements (blue shaded area) in the enriched region, containing the fined mesh with an elemental nodal distance of 0.2 mm, for a crack growth analysis of the current study. Full integration was used instead of reduced integration for more accurate stress computation of the highly distorted elements in the weld region. A mesh sensitivity study was performed to determine an appropriate element size for all models discussed in Sections 3.1, 3.2 and 3.3.

The conductivity, density and coefficient of thermal expansion were adopted from [23]. The specific heat can reach very high values at certain temperatures for which a simplified curve is usually implemented in weld process simulations. A comparison was made among the specific heat curves of various researchers [19,23–27], each using different peak values at phase transformations. The specific heat curve was adopted from Perić et al. [19]. However, due to significant differences reported, a sensitivity study was conducted. The adopted material properties are presented in Fig. 4. The Stefan–Boltzmann constant ($5.672 \cdot 10^{-8}$ W m^{-2} K^{-4}) was included and the emissivity and heat transfer coefficient were set to 0.9 and 10 W m^{-2} K^{-1}, respectively, following Perić et al. [19]. The surrounding temperature was set to 20 °C. Phase transformations were not included in the simulations as it has shown to have minor influence on the residual stress for loosely supported specimens. Note that phase transformations influence the thermal deformations and therefore also the residual stress in the case the specimen is constrained [28]. The Young's modulus and Poisson's ratio were adopted from [23]. The true stress–strain curves utilised in the model were adopted from [23], where they were experimentally determined for various temperatures. Isotropic hardening was used, maintaining a small positive slope beyond the tensile strength. The resulting stress did not exceed the plastic strain of 0.2 in any Gauss point. These curves are depicted in Fig. 5. A distinction between the properties of the base material, heat affected zone and weld was not made.

2.2. Welding simulation

The finite element models of the current study simulate the spray transfer MAG welding process, commonly used for the selection of plate thicknesses considered in this study. Various models have been proposed in the literature to simulate the welding heat source. Rosenthal [29,30] and Rykalin [31] proposed a concentrated source while Pavelic et al. [32] proposed a distributed source with a Gaussian distribution. The current study adopted the double ellipsoidal heat source distribution proposed by Goldak [33]. Eqs. (1)–(3) provide the power density distributions for the distributions in front and at the rear of the heat source, denoted with

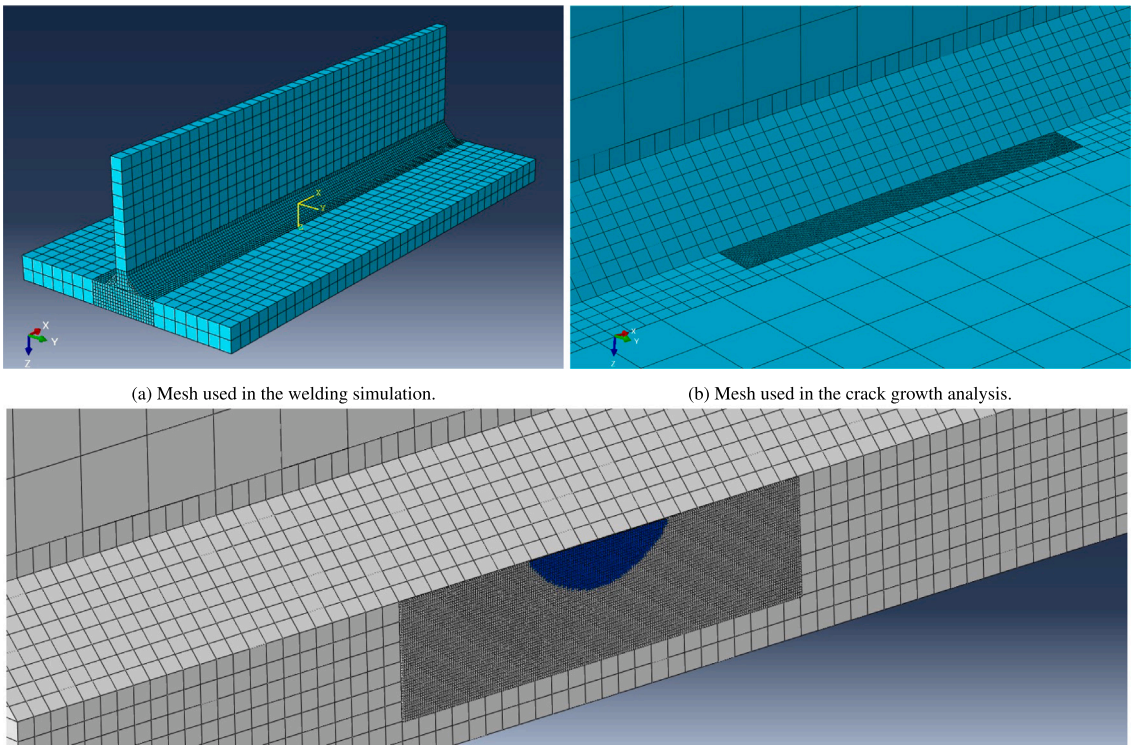

(a) Mesh used in the welding simulation.

(b) Mesh used in the crack growth analysis.

(c) Cracked elements in enriched region.

Fig. 3. Isometric view of the model.

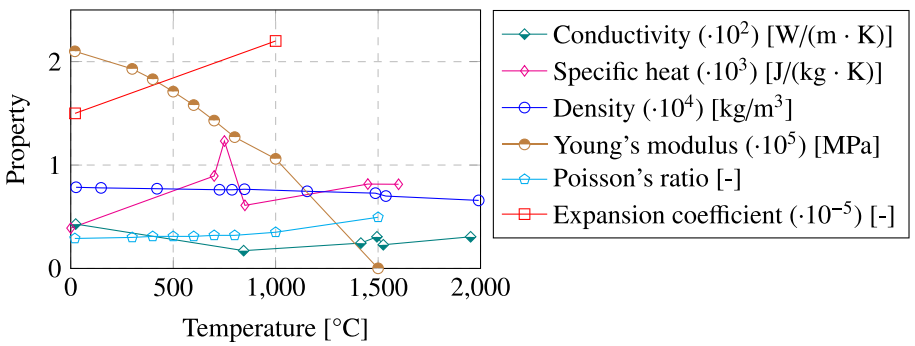

Fig. 4. Temperature dependent material properties.
Source: Data from [19,23].

q_f and q_r, respectively. A local travelling coordinate system ($X_{L,h}$, $Y_{L,h}$ and $Z_{L,h}$) was adopted, with the torch as the origin. Fig. 6 visualises the Goldak double ellipsoid [33].

$$q_f(X_{L,h}, Y_{L,h}, Z_{L,h}) = Q \cdot \frac{6 \cdot \sqrt{3} \cdot f_1}{b \cdot d \cdot \pi \cdot \sqrt{\pi} \cdot c_1} \cdot e^{-3 \cdot [(\frac{X_{L,h}}{c_1})^2 + (\frac{Y_{L,h}}{b})^2 + (\frac{Z_{L,h}}{d})^2]} \tag{1}$$

$$q_r(X_{L,h}, Y_{L,h}, Z_{L,h}) = Q \cdot \frac{6 \cdot \sqrt{3} \cdot f_2}{b \cdot d \cdot \pi \cdot \sqrt{\pi} \cdot c_2} \cdot e^{-3 \cdot [(\frac{X_{L,h}}{c_2})^2 + (\frac{Y_{L,h}}{b})^2 + (\frac{Z_{L,h}}{d})^2]} \tag{2}$$

$$Q = \eta \cdot U \cdot I \tag{3}$$

In these equations, the power input (Q) was described as the product of the efficiency (η), voltage (U) and amperage (I). Typical values for MAG welding procedure were adopted from [34]. The shape of the double ellipsoid heat source was determined by the half-width (b), depth (d) front length (c_1) and rear length (c_2). These shape parameters are typically derived from weld pool

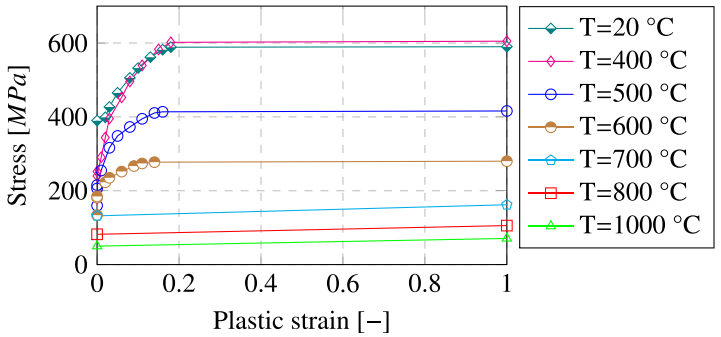

Fig. 5. Stress strain curves for various temperatures.
Source: Data from [23].

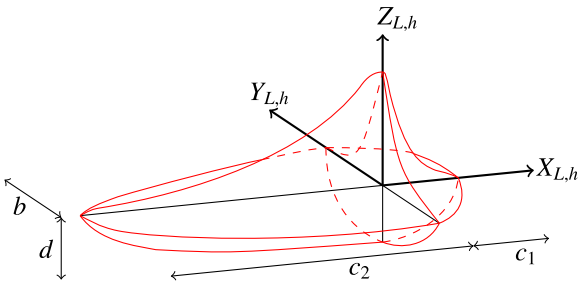

Fig. 6. Goldak heat source model.

measurements [35]. The heat deposited fractions for the front and rear parts, denoted as f_1 and f_2 respectively, were described by $f_1 = \frac{2c_1}{c_1+c_2}$, $f_2 = \frac{2c_2}{c_1+c_2}$ [36]. Section 3 gives the selected values. The heat source was rotated 45° with respect to the global X-axis.

The heat source was applied using the Dflux subroutine in Abaqus/CAE 2022. The birth/death principle, as described in [37–39], was applied in the simulation to account for the added filler material during the welding process. Initially, all elements describing the welds were deactivated. They were then activated incrementally as the heat source passed through. To limit computational expenses, activation occurred for a batch of elements simultaneously. Ten increments per weld pass were used to reactivate the elements in the weld. The elements of the next weld increment were introduced when the heat source was at the beginning of that particular increment. Tack welds are often applied before creating a long fillet weld, serving as constraints for the final welding procedure. In some of the simulations, tack welds were modelled in an approximate way by activating the elements of the first and last weld increment of each pass before applying the heat source. Fig. 7 illustrates the birth/death principle with the travelling heat source.

2.3. Crack growth simulation

While the total fatigue life of the structure comprises the crack initiation stage, short crack growth stage and the long crack growth stage, the current research was focused on the long crack growth stage only. As a result, the effect of the residual stresses on the shape of the crack, as well as the redistribution of these stresses during the stages preceding the long crack growth, were not considered. The crack was inserted at the location of the highest transverse residual stress along pass 1 (see Fig. 2) of the reference case indicated in Section 3.2. This was located at an X-coordinate of −56.25 mm, as can be seen in Fig. 16. The von Mises stresses at the location of the crack were investigated to support the use of linear elastic fracture mechanics. Only a small region close to the crack front was above yielding and this region was small compared to the crack size, to such an extent that the generally accepted condition for linear elastic fracture mechanics analysis was satisfied. For the entire crack growth analysis, the radius of the plastic zone around the crack front was analysed. In the case of maximum stress intensity factor, this analysis revealed that the ratio of the radius of the plastic zone at the crack front to the crack depth remained below 1/8 (i.e. $r_y/a < 1/8$), which supports the use of linear elastic fracture mechanics. An initial crack with a semi-elliptical shape, as illustrated in Fig. 8, was subsequently inserted with a crack depth (a) and crack length ($2c$) of 0.75 mm and 3 mm, respectively. The crack was located in the base plate at the weld toe and oriented in the XZ-plane using the coordinate system presented in Fig. 3. The extended finite element method (XFEM) was used in which stationary cracks were assessed. The stress intensity factors were carefully analysed, revealing convergence for contours 2 through 10, from which the mean average was used. Fig. 9 shows the evolution of the stress intensity factor range of each mode throughout the crack growth analysis for the deepest point of the crack (i.e. $\theta = 90°$). From this figure it is concluded that the studied crack was dominated by Mode I, therefore Modes II and III were neglected in the analysis.

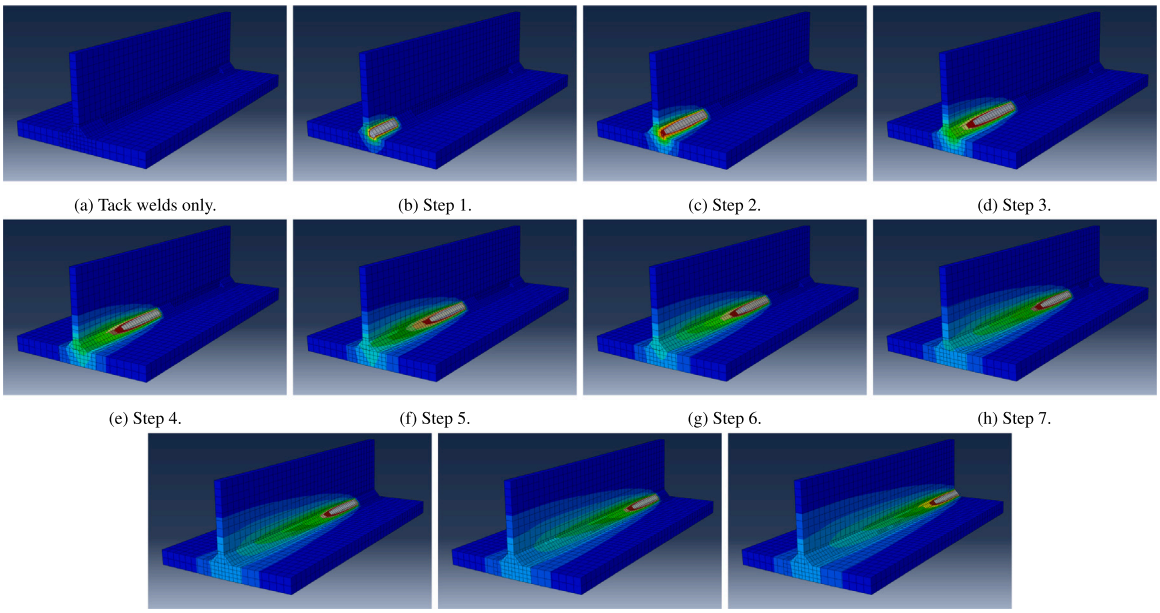

(a) Tack welds only. (b) Step 1. (c) Step 2. (d) Step 3.

(e) Step 4. (f) Step 5. (g) Step 6. (h) Step 7.

(i) Step 8. (j) Step 9. (k) Step 10.

Fig. 7. Welding simulation steps of Pass 1 with temperature distribution indicated by contour plots.

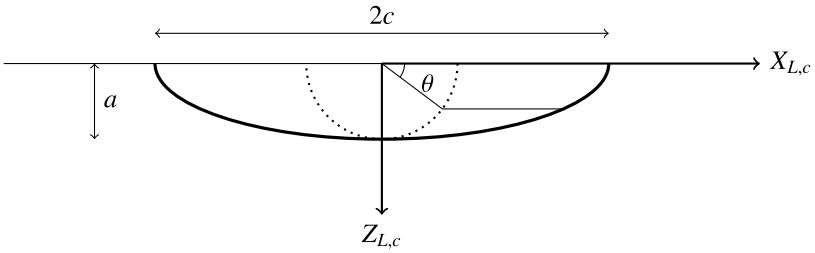

Fig. 8. Illustration of surface crack.

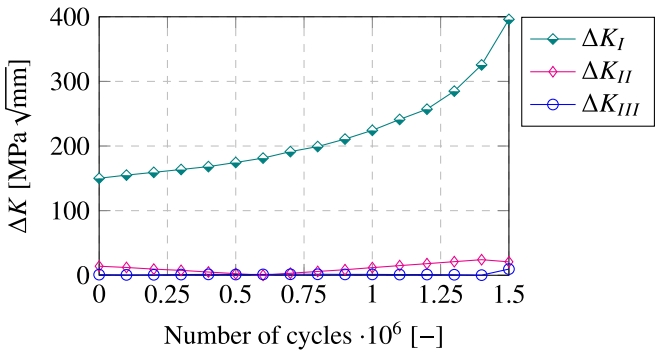

Fig. 9. Stress intensity factor range for each mode at the deepest point of the crack throughout the crack growth analysis.

The minimum stress intensity factor (K_{min}) was described by the stress intensity factor resulting from the residual stresses and the minimum value of the external loading, as presented in Eq. (4). The maximum stress intensity factor (K_{max}) was described by the stress intensity factor resulting from the residual stresses and the maximum value of the external loading, as presented in Eq. (5) [11,17,40]. The effective stress intensity factor ratio R_{eff} was defined as the minimum stress intensity factor K_{min} divided by the maximum stress intensity factor K_{max}, as shown in Eq. (6). The externally applied stress ratio R was defined as the minimum applied stress σ_{min} divided by the maximum applied stress σ_{max}, as shown in Eq. (7). Finally, the stress intensity factor range ΔK

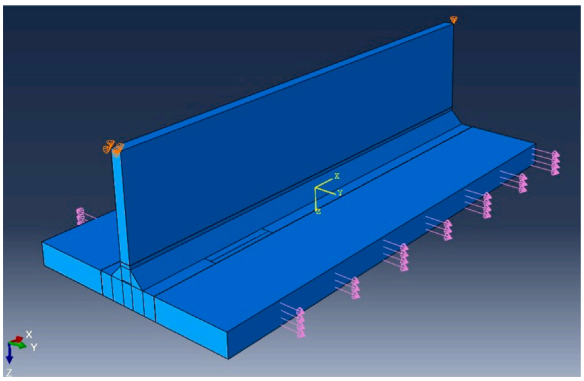

Fig. 10. T-joint model with loading conditions.

was defined as the difference between K_{max} and K_{min}, as shown in Eq. (8).

$$K_{min} = K_{RS+L_{min}} \tag{4}$$

$$K_{max} = K_{RS+L_{max}} \tag{5}$$

$$R_{eff} = \frac{K_{min}}{K_{max}} \tag{6}$$

$$R = \frac{\sigma_{min}}{\sigma_{max}} \tag{7}$$

$$\Delta K = K_{max} - K_{min} \tag{8}$$

The Walker equation [41] was selected to take into account the stress ratio on the crack propagation rate, following Eq. (9).

$$\frac{da}{dn} = C \cdot \left[\frac{\Delta K_I}{(1 - R_{eff})^{1-\gamma}} \right]^m \tag{9}$$

The empirical constants from the Paris equation [42] were adopted from the BS7910 [43], i.e. $C = 3.98 \cdot 10^{-13}$ and $m = 2.88$. The constant γ in the Walker equation was selected as 0.76, following [44]. The base plate was loaded at the surfaces indicated in Fig. 10 with a stress range of 100 MPa with an external stress ratio of 0.

In order to study fatigue crack propagation behaviour, a stepwise crack growth analysis was performed using a discrete number of steps, each involving $\Delta n = 100{,}000$ load cycles, where the crack front was updated in each step. A 2nd order polynomial was fitted through the coordinates of each crack front node and its two adjacent nodes. The crack front node was assumed to propagate normal to this 2nd order polynomial at the location of the centre node. This process was repeated for each crack front node to obtain the new crack shape. The new (updated) crack front was subsequently smoothed by regression using a 6th order polynomial involving the coordinates of all extended crack front nodes. The process of updating the crack front is illustrated in Fig. 11. During the crack growth analysis, the stress intensity factors were analysed to ensure that the difference with the stress intensity factors of the previous crack remained smaller than 5%. A local coordinate system ($X_{L,c}$ and $Z_{L,c}$) was used which was placed at the surface point halfway the length of the crack.

3. Results

3.1. Verification and validation of residual stress simulations

The thermal and mechanical models, used for obtaining welding-induced residual stresses, were validated by comparing the resulting residual stress with those from other experimental and numerical studies [18,19,21]. Other studies [22,45] were not included because of incomplete information on geometry or weld parameters. Welding parameters (welding speed v, voltage U and electric current I) and geometrical parameters were adopted from each study, see Tables 1 and 2, respectively. Tack welds were not modelled in the models for validation.

Fig. 12 presents the locations where the residual stresses are presented in this section. Path 1 and 2 are located halfway along the length of the specimen, with path 2 situated at the surface of the base plate closest to the attachment, while path 1 is located on the opposing side.

Bhatti et al. [18] conducted a welding experiment on a T-joint of steel grade S355. The gas metal arc welding (GMAW) process was used and welding of Pass 2 was performed in the opposite direction of Pass 1, as indicated in Fig. 12. To prevent movement

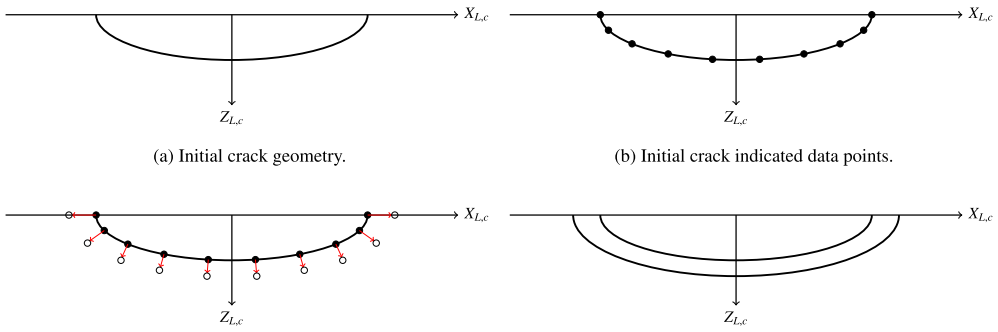

(a) Initial crack geometry.

(b) Initial crack indicated data points.

(c) New positions corresponding to initial crack data points.

(d) New crack geometry.

Fig. 11. Incremental crack growth methodology for planar surface cracks.

Table 1
Overview geometrical properties, see Fig. 2 for symbols definition.

Ref.	L [mm]	W [mm]	H [mm]	T_B [mm]	T_S [mm]	H_W [mm]	W_W [mm]
Bhatti [18]	130	300	50	6	6	6	6
Peric [21]	500	300	300	10	10	7	7
Peric [19]	350	150	150	15	15	10	10

Table 2
Overview welding parameters.

Ref.	η [–]	v [mm/s]	U [V]	I [A]
Bhatti [18]	0.85	8.30	30	290
Peric [21]	0.83	6.67	29	270
Peric [19]	0.85	6.73	41	540

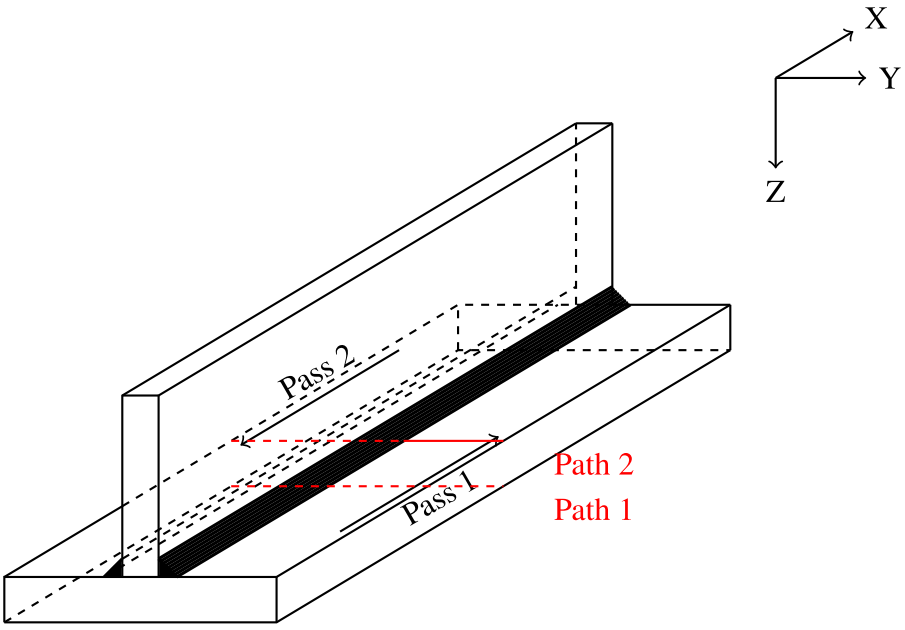

Fig. 12. Locations along which residual stresses are presented for validation.

during welding, the edge closest to the first weld pass was clamped. Residual stresses were measured in the transverse direction (perpendicular to the welding direction) using X-ray diffraction along path 2 (as per Fig. 12). Zhu et al. [20] conducted a numerical

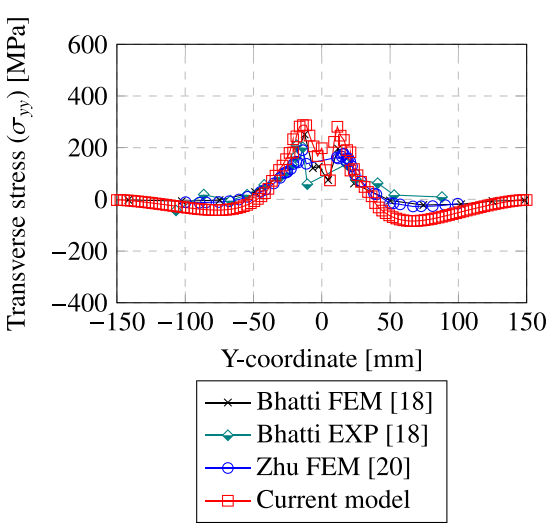

(a) Transverse residual stress following [18] and [20].

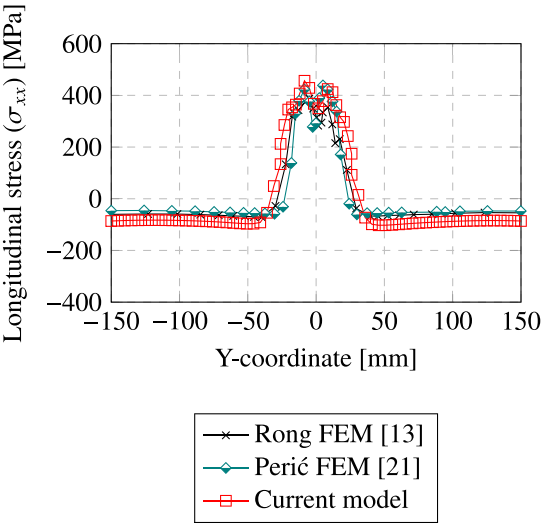

(b) Longitudinal residual stress following [13] and [21].

Fig. 13. Validation of welding-induced residual stresses along path 2, as per Fig. 12.

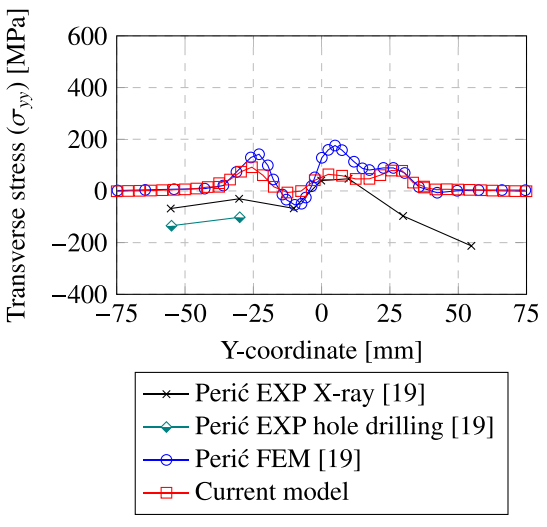

(a) Transverse residual stresses following [19].

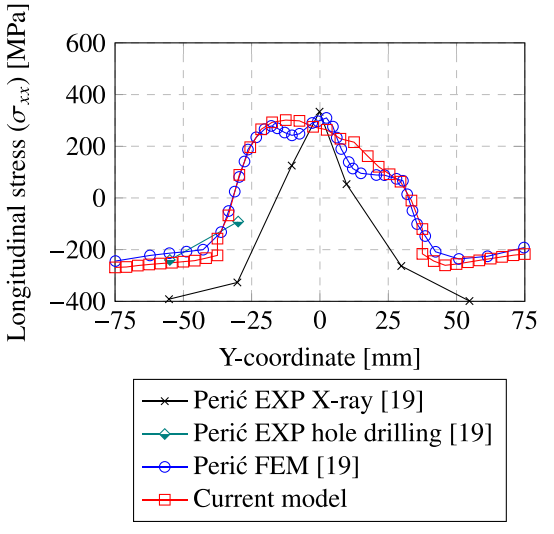

(b) Longitudinal residual stresses following [19].

Fig. 14. Validation of welding-induced residual stresses along path 1, as per Fig. 12.

study and validated their results with the experimental measurements from Bhatti et al. [18]. Fig. 13(a) presents the residual stress resulting from the experiment and from the numerical simulations.

Perić et al. [21] conducted a welding experiment on a T-joint of steel grade S355. Metal active gas (MAG) welding was used and Passes 1 and 2 were again applied in opposite directions. While no movement restrictions were specified in the experiments, translation restrictions were modelled at all 4 corners of the base plate as per Figure 1 of [21]. Although residual stresses were not measured, a finite element model was composed by Perić et al. [21] from which the longitudinal residual stresses (in welding direction) along path 2 (as per Fig. 12), were extracted and reported. Rong et al. [13] conducted a similar finite element analysis using the conditions from [21]. Fig. 13(b) presents the residual stresses resulting from the experiment and the simulations.

Perić et al. [19] conducted a welding experiment on a T-joint of steel grade S355. The plates were not restricted from deformation. The plates were welded using the submerged arc welding process and Passes 1 and 2 were again applied in opposite directions. Surface residual stresses were measured using X-ray diffraction and hole drilling method at the bottom surface of the base plate, halfway the specimen length (along path 2, as per Fig. 12). Both the transverse and the longitudinal residual stresses were measured. The results are presented in Figs. 14(a) and 14(b).

Table 3
Overview geometrical properties with the reference values within brackets, see Fig. 2 for symbols definition.

L [mm]	W [mm]	H [mm]	T_B [mm]	T_S [mm]	H_W [mm]	W_W [mm]
100–300 (200)	100–300 (100)	50	10–30 (10)	5	6	6

Table 4
Welding variables with Goldak heat source parameters with the reference values within brackets, see Fig. 6 for symbols definition.

b [mm]	d [mm]	c_1 [mm]	c_2 [mm]	η [–]	U [V]	I [A]	v [mm/s]
3	3	3	6	0.8	25	250	6.67

Table 5
Welding variables utilised in the sensitivity study towards the base plate thickness, see Figs. 2 and 6 for symbols definition.

T_B [mm]	U [V]	I [A]	v [mm/s]
10	25	250	6.67
20	27	270	8.00
30	29	290	10.00

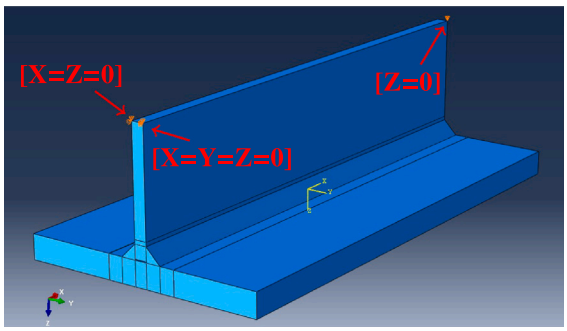

Fig. 15. T-joint model with boundary conditions.

The simulation results of the current model have been added to Figs. 13 and 14. A reasonable agreement follows between the experiment and the numerical simulations. Given these observations, the current model was considered appropriate for further analyses.

3.2. Sensitivity study

A sensitivity study was conducted to assess the influence of the geometrical parameters. Tables 3 and 4 provide the reference values used in the current study. The double ellipsoid parameters of the Goldak heat source [33], corresponding to the size of the weld following [35], are illustrated in Fig. 6. The values presented within brackets represent the values used for the reference model. Tack welds were modelled in the following models, as explained in Section 2.2. The interpass time was set to 200 s and a cooling time of 5000s was applied after finishing the second weld pass to ensure sufficient cooling for the formation of residual stresses. One pass was considered on both sides of the T-joint for all simulations in the order as illustrated in Fig. 2. In the sensitivity study towards the base plate thickness, different welding parameters were used to maintain realistic welding scenarios. The corresponding parameters are presented in Table 5.

The plates were considered unconstrained (e.g. unclamped) during the welding procedure. Therefore, minimal boundary conditions were applied in the mechanical model to prevent rigid body translation and rotation. The reaction forces were checked to be close to 0N. Fig. 15 presents the applied boundary conditions.

Fig. 16 presents the results of the sensitivity study in terms of the transverse residual stress along the weld toe of Pass 1 (as indicated in Fig. 2). A clear influence of the connection geometry is demonstrated. Increasing the base plate thickness and width led to higher constraints during weld shrinkage which resulted in higher residual stresses. The peak residual stresses in case of a base plate thickness of 30 mm were two times higher compared to a base plate of 10 mm. Similar as observed by [18,21], where a base plate width of 300 mm was used, relatively high tensile stresses were obtained halfway the specimen length. Varying the specimen length led to a change in location of peak stresses. The peak tensile residual stress was located at 25% and 17% of the plate edges

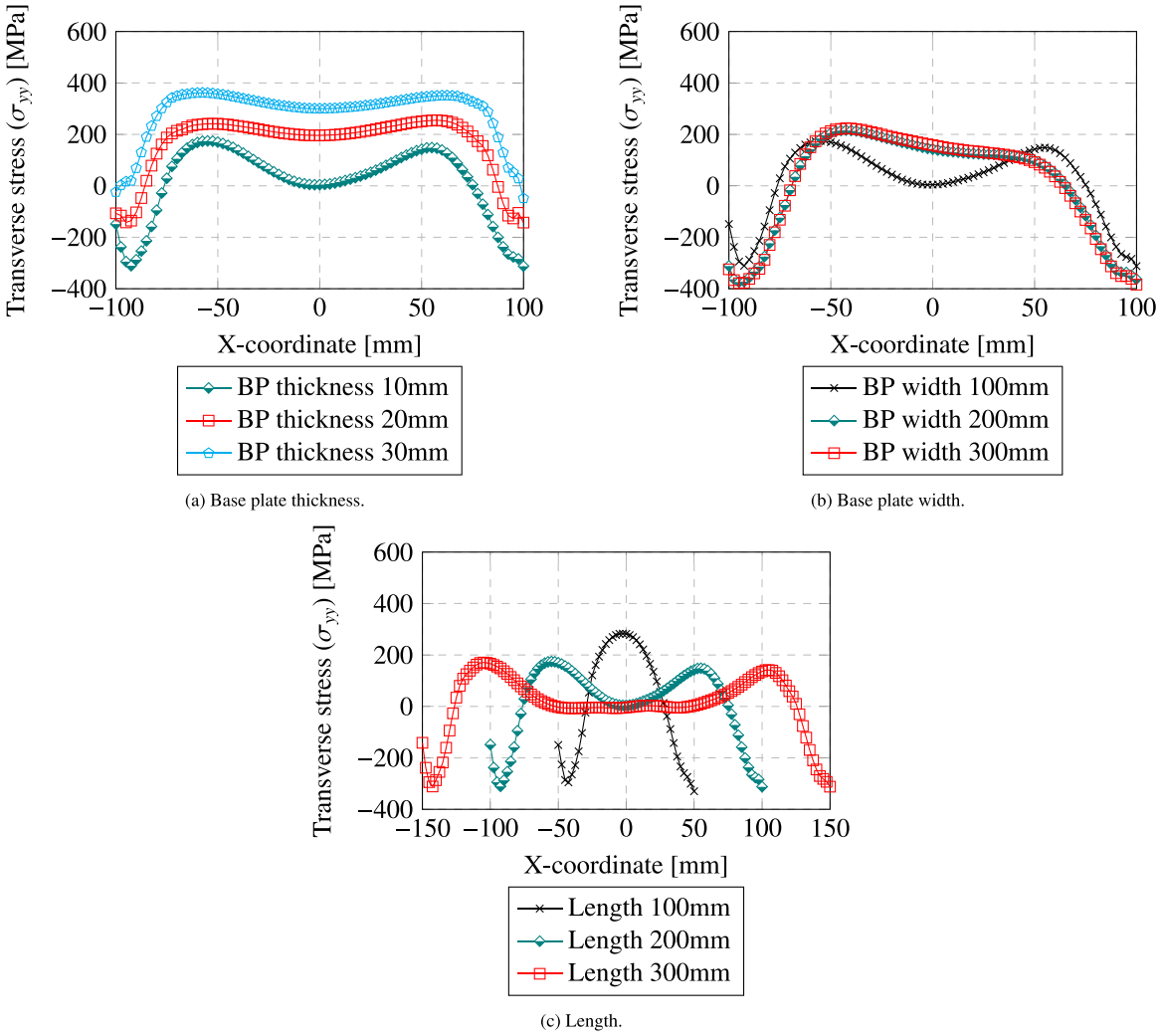

(a) Base plate thickness.

(b) Base plate width.

(c) Length.

Fig. 16. Transverse residual stress at the weld toe of Pass 2 for the sensitivity study (BP = Base plate).

for the case of a specimen length of 300 mm and 200 mm, respectively. In the case of a length of 100 mm, the peak tensile residual stress was found halfway the length.

3.3. Crack growth in residual stress field

The geometrical and welding parameters listed in Tables 3 and 4 were used in the analysis presented in this section. Figs. 17(a) and 17(b) show the resulting crack growth without and with welding-induced residual stresses, respectively. A stress ratio of the externally applied load equal to $R = 0$ was used for both cases. The results are presented for each 2nd crack increment, starting from the initial crack and ending at increment 10, where each increment consists of 100,000 loading cycles.

After 14 increments, the growth in depth direction and the growth in length direction in the simulation with the effects of welding-induced residual stresses were 286% and 473% larger respectively, compared to those of the simulation without residual stress. Additional simulations were run for external stress ratios of $R = 0.5$ and $R = -1$ without residual stress and for external stress ratios of $R = -1$ with residual stress. Fig. 18 presents the cumulative number of cycles plotted against the crack length and crack depth for the aforementioned simulations. The impact of residual stresses on the crack length and depth is significant. Only the simulation without residual stresses, using an external stress ratio of 0.5, approximated the crack growth observed in simulations with residual stresses.

Fig. 19 presents the crack growth curves for the analyses with and without welding-induced residual stress for various external stress ratios. As expected, the effect of stress ratio of externally applied load, R, on crack growth rate with residual stress was smaller compared to that without residual stress. This finding aligns with experimental research [46]. Furthermore, the crack growth rate

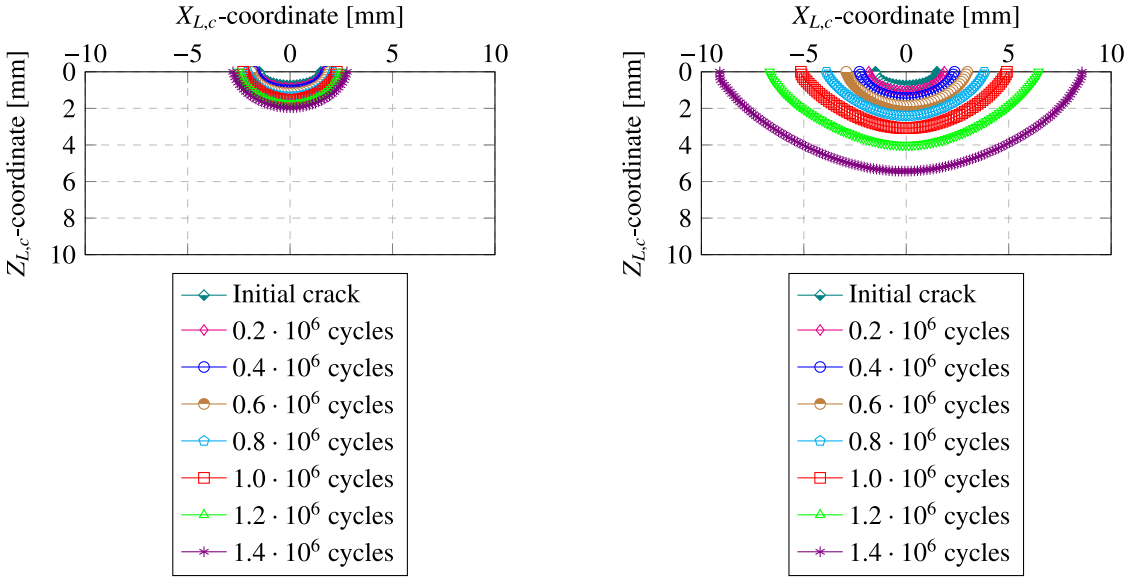

(a) Without residual stress. (b) with residual stress.

Fig. 17. Crack front extension for a stress range $\Delta\sigma = 100$ MPa at external stress ratio R = 0 in a body without (a) and with (b) residual stress.

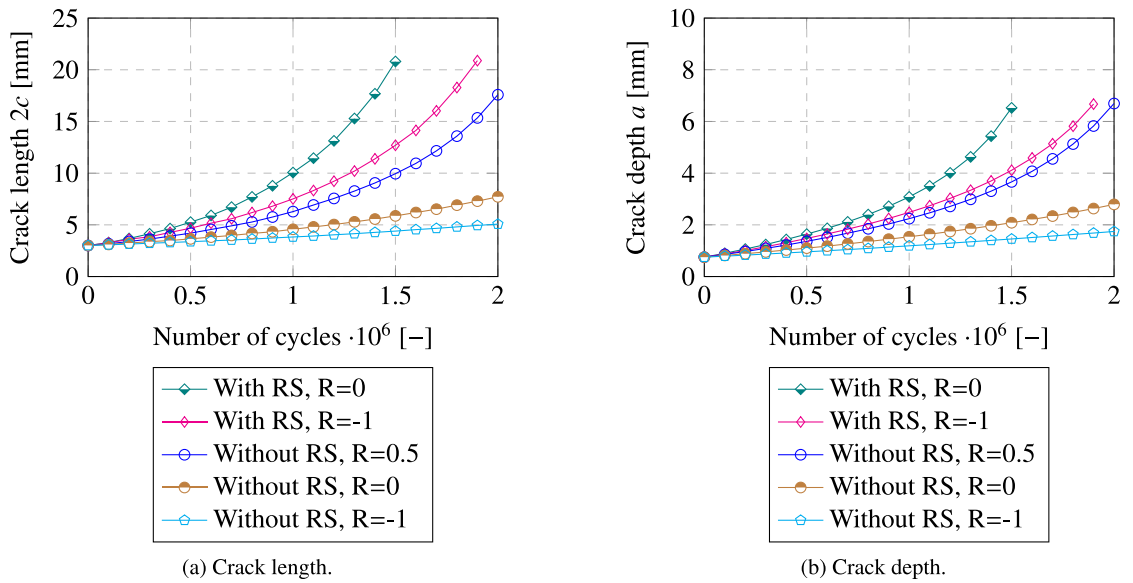

(a) Crack length. (b) Crack depth.

Fig. 18. Effect of welding-induced residual stresses on crack length (a) and crack depth (b) for a stress range $\Delta\sigma = 100$ MPa at various external stress ratios.

with residual stress at any external stress ratio was closely aligned with the crack growth rate without residual stress at high stress ratio. This numerical result is in agreement with test data from [47,48]. When analysing welding-induced residual stress, it was found that the minimum stress intensity factor consistently remained positive, even in cases of a load ratio of the external load of $R = -1$. The effective stress intensity factor ratio is plotted along the crack front for various crack increments for the simulations with residual stresses with $R = 0$ in Fig. 20(a) and $R = -1$ in Fig. 20(b). The position along the crack front is denoted by the projected ellipsoidal angle, θ, as defined in Fig. 8. Both graphs show that the effective stress intensity factor ratio had a value of approximately 0.6 along the crack front throughout the entire simulation, but it decreased slightly at the deepest point as the crack grew.

Fig. 21 presents the redistribution of the transverse residual stresses in thickness direction along the $Z_{L,c}$ axis as presented in Fig. 8. Additionally, the residual stress field in the uncracked body is presented as well as the residual stress field described in [49] and implemented in BS7910 [43]. Extrapolation of the redistributed residual stresses was used from the nodal value closest to the

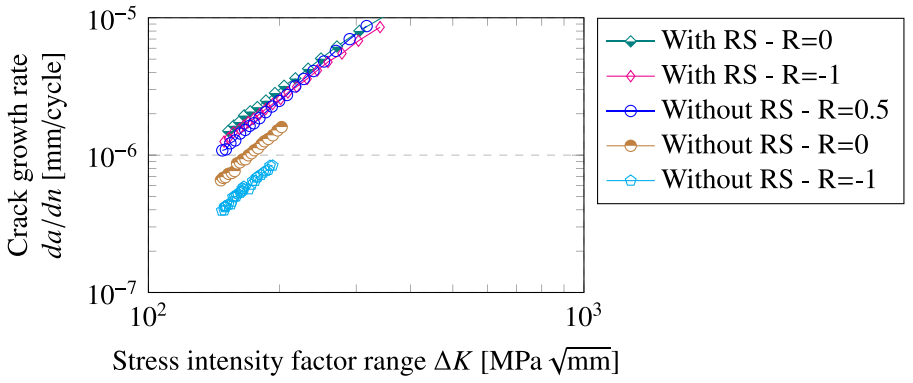

Fig. 19. Crack growth curves.

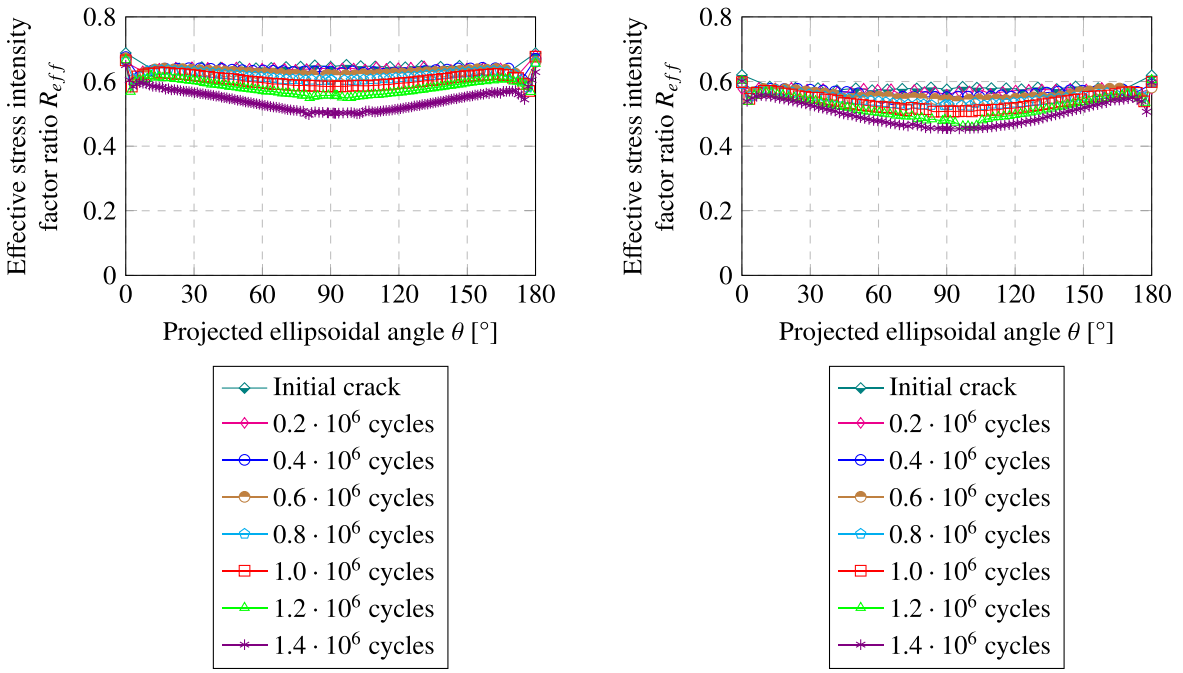

(a) External stress ratio $R = 0$.

(b) External stress ratio $R = -1$.

Fig. 20. Distribution of effective stress intensity factor ratio R_{eff} along the crack front for a stress range $\Delta\sigma = 100$ MPa at external stress ratio $R = 0$ (a) and $R = -1$ (b).

crack front towards the crack front. This is indicated by the dotted lines. At the considered location, the transverse residual stresses were in tension over the entire thickness. As welding induced residual stress is self-balancing, these tensile stresses were compensated by compressive stresses at the edges of the plate. Due to the presence of the crack, the geometry deformed and this caused an increase of stresses at the crack front. As the crack grew, the residual stress at the crack front remained at a high (tensile) value, despite the residual stress decaying in the depth direction in the uncracked body. This finding aligns with the experimental measurements on a through-thickness crack by Servetti et al. [15]. The current simulation shows how the residual stress field redistributed as the crack grew. Fig. 22 presents the redistribution of the transverse residual stresses along the weld toe of Pass 1 (see Fig. 2). A similar trend was found at the surface points of the crack were the redistributed residual stresses were found to be higher than the initial residual stresses without the crack.

Fig. 23 shows the stress intensity factor, resulting from welding-induced residual stresses in the current model, plotted for the deepest point of the crack. Additionally, the weight function method (WFM) [50] was used in which the residual stresses were described by a polynomial function, following [51]. Both the linear trend of the residual stress, as described in [49] and included in BS7910 [43], and the trend from the current welding simulation were analysed using the WFM. The results show that linear decaying residual stress, as described by BS7910 [43], provides stress intensity factors that are conservative for the studied case.

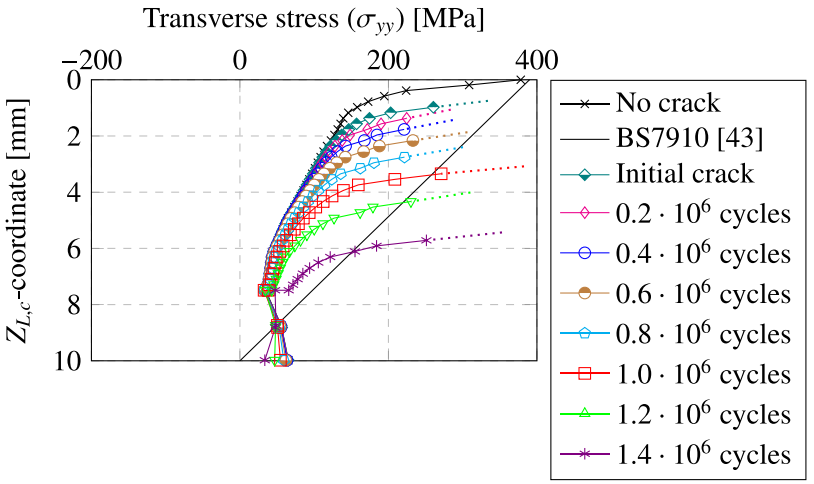

Fig. 21. Redistribution of transverse residual stresses through thickness of the base plate due to crack growth.

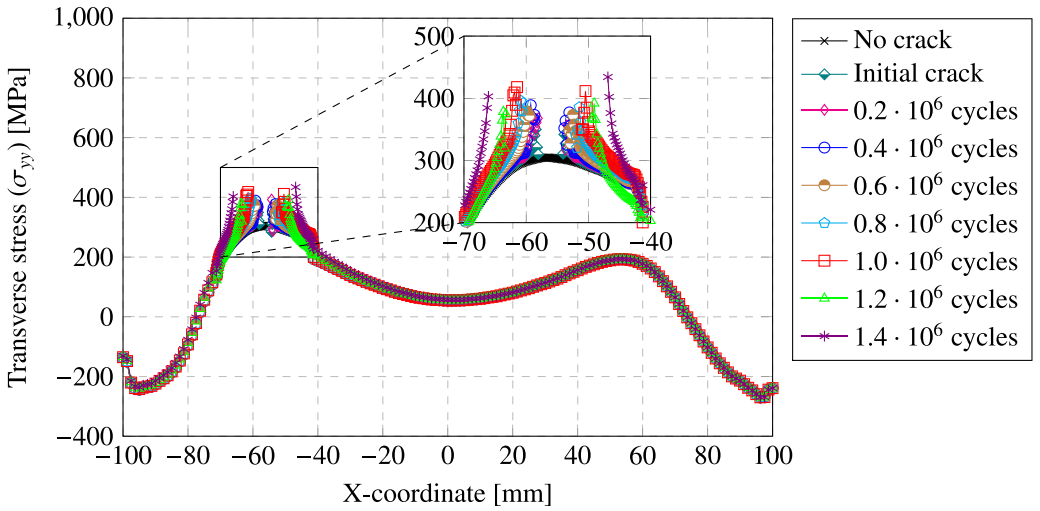

Fig. 22. Redistribution of transverse residual stresses along the weld toe of weld Pass 1 (see Fig. 2) due to crack growth.

This results from the description of the residual stress field in the uncracked state where the residual stress in the current model is significantly lower than the linear description provided by the BS7910 [43]. Finally, a good agreement was found between the results from the current model and the WFM where the description of the residual stress from the current model was implemented. As the weight function method is unable to account for deformations of the whole body, this implies that the deformation changes due to a growing crack have limited influence on the stress intensity factor for the studies case at the deepest point of the crack. However, these deformations cause the stress at the surface point to increase with increasing crack size as shown in Fig. 22. These results show that the more detailed description of the residual stress field had a significant influence on the stress intensity factor.

4. Concluding remarks

A welding simulation was performed to determine the influence of the welding-induced residual stresses in a T-joint for different geometry and welding parameters. The methodology was validated by FE-results and with experimental measurements from various other studies available in literature. A subsequent crack growth simulation was performed to study the effect of the welding-induced residual stresses on crack growth and the effect of crack growth on the redistribution of the residual stresses. The main conclusions are:

- Increasing the base plate thickness led to a significant increase in transverse residual stress due to the higher constraints during weld shrinkage. The peak residual stress was two times higher for a 30 mm thick plate than a 10 mm thick plate.

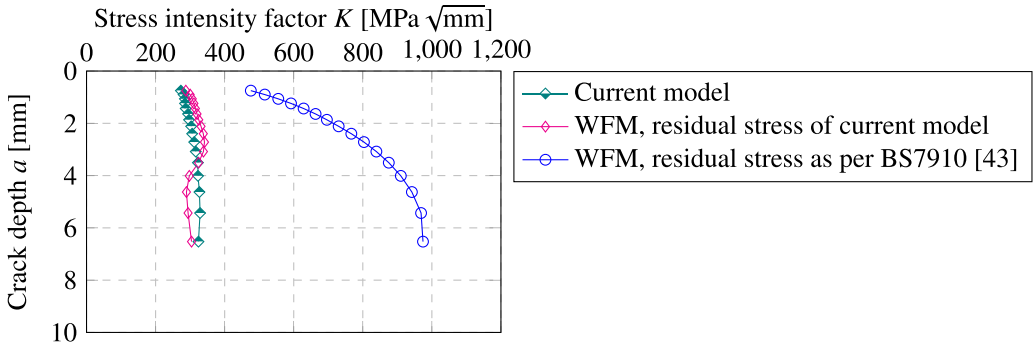

Fig. 23. Comparison of the stress intensity factor due to welding-induced residual stresses of the current model with BS7910 [43].

- Varying the length of the specimen resulted in a change in the location of the peak transverse residual stress. The tensile residual stress peak was located at 17% and 25% of the plate edges for specimen lengths of 200 mm and 300 mm, respectively.
- The external stress ratio did not significantly influence the crack growth rate in the presence of welding-induced residual stresses. While varying the external stress ratio, the effective stress intensity factor ratio of the model including residual stresses remained at an almost constant value of approximately 0.6 for the geometry considered.
- The residual stress field changed as the crack grew, in such a way that the stress at the deepest point of the crack remained approximately equal in the model prediction.
- There was a significant difference between the stress intensity factor due to residual stress of the current model and the formulation outlined in BS7910. The detailed description of the residual stress field of the current model led to lower stress intensity factors. The stress intensity factors due to residual stress can be accurately estimated with the weight function method for the studied geometry.

CRediT authorship contribution statement

David Malschaert: Writing – original draft. **Milan Veljkovic:** Writing – review & editing, Supervision. **Johan Maljaars:** Writing – review & editing, Supervision.

Declaration of competing interest

The authors declare that they have no known competing financial interests or personal relationships that could have appeared to influence the work reported in this paper.

Data availability

Data will be made available on request.

Acknowledgements

This research was carried out under project number T20006c in the framework of the Research Program of the Materials innovation institute, Netherlands (M2i) (www.m2i.nl) supported by Rijkswaterstaat and ProRail.

References

[1] Zerbst U, Ainsworth R, Beier HT, Pisarski H, Zhang Z, Nikbin K, Nitschke-Pagel T, Münstermann S, Kucharczyk P, Klingbeil D. Review on fracture and crack propagation in weldments–A fracture mechanics perspective. Eng Fract Mech 2014;132:200–76. http://dx.doi.org/10.1016/j.engfracmech.2014.05.012.
[2] Zerbst U. Application of fracture mechanics to welds with crack origin at the weld toe: A review part 1: Consequences of inhomogeneous microstructure for materials testing and failure assessment. Weld World 2019;63(6):1715–32. http://dx.doi.org/10.1007/s40194-019-00801-5.
[3] Chen S, Guo M, Li Y, Dong X, He J. Effects of residual stresses on fatigue crack propagation of T-joint using extended finite element method (XFEM). Metals 2022;12(8):1368. http://dx.doi.org/10.3390/met12081368.
[4] Zhang W, Jiang W, Zhao X, Tu S-T. Fatigue life of a dissimilar welded joint considering the weld residual stress: Experimental and finite element simulation. Int J Fatigue 2018;109:182–90. http://dx.doi.org/10.1016/j.ijfatigue.2018.01.002.
[5] Lee C-H, Chang K-H, Van Do VN. Modeling the high cycle fatigue behavior of T-joint fillet welds considering weld-induced residual stresses based on continuum damage mechanics. Eng Struct 2016;125:205–16. http://dx.doi.org/10.1016/j.engstruct.2016.07.002.
[6] Wang D, Zhang H, Gong B, Deng C. Residual stress effects on fatigue behaviour of welded T-joint: a finite fracture mechanics approach. Mater Des 2016;91:211–7. http://dx.doi.org/10.1016/j.matdes.2015.11.106.
[7] Spyridoni K, Xin H, Hermans M, Veljkovic M. Calibration of welding simulation parameters of fillet welding joints used in an orthotropic steel deck. CE Pap 2019;3(3–4):49–54. http://dx.doi.org/10.1002/cepa.1089.

[8] Hensel J. Mean stress correction in fatigue design under consideration of welding residual stress. Weld World 2020;64(3):535–44. http://dx.doi.org/10.1007/s40194-020-00852-z.
[9] ISO. Welding - quality requirements for heat treatment in connection with welding and allied processes. Int Organ Stand 2009. ISO 17663:2009 en.
[10] Marquis GB, Barsoum Z. IIW recommendations on high frequency mechanical impact (HFMI) treatment for improving the fatigue strength of welded joints. In: IIW recommendations for the HFMI treatment. Springer; 2016, p. 1–34.
[11] Zerbst U. Application of fracture mechanics to welds with crack origin at the weld toe—a review. Part 2: welding residual stresses. Residual and total life assessment. Weld World 2020;64(1):151–69. http://dx.doi.org/10.1007/s40194-019-00816-y.
[12] Chen Q, Fei F, Yu S, Liu C, Tang J, Yang X. Numerical simulation of temperature field and residual stresses in stainless steel T-joint. Trans Indian Inst Met 2020;73(3):751–61. http://dx.doi.org/10.1007/s12666-020-01890-3.
[13] Rong Y, Zhang G, Huang Y. Study of welding distortion and residual stress considering nonlinear yield stress curves and multi-constraint equations. J Mater Eng Perform 2016;25(10):4484–94. http://dx.doi.org/10.1007/s11665-016-2259-1.
[14] Hensel J, Nitschke-Pagel T, Ngoula DT, Beier H-T, Tchuindjang D, Zerbst U. Welding residual stresses as needed for the prediction of fatigue crack propagation and fatigue strength. Eng Fract Mech 2018;198:123–41. http://dx.doi.org/10.1016/j.engfracmech.2017.10.024.
[15] Servetti G, Zhang X. Predicting fatigue crack growth rate in a welded butt joint: The role of effective R ratio in accounting for residual stress effect. Eng Fract Mech 2009;76(11):1589–602. http://dx.doi.org/10.1016/j.engfracmech.2009.02.015.
[16] Liljedahl C, Tan M, Zanellato O, Ganguly S, Fitzpatrick M, Edwards L. Evolution of residual stresses with fatigue loading and subsequent crack growth in a welded aluminium alloy middle tension specimen. Eng Fract Mech 2008;75(13):3881–94. http://dx.doi.org/10.1016/j.engfracmech.2008.02.005.
[17] Liljedahl C, Zanellato O, Fitzpatrick M, Lin J, Edwards L. The effect of weld residual stresses and their re-distribution with crack growth during fatigue under constant amplitude loading. Int J Fatigue 2010;32(4):735–43. http://dx.doi.org/10.1016/j.ijfatigue.2009.10.012.
[18] Bhatti AA, Barsoum Z, Murakawa H, Barsoum I. Influence of thermo-mechanical material properties of different steel grades on welding residual stresses and angular distortion. Mater Des (1980-2015) 2015;65:878–89. http://dx.doi.org/10.1016/j.matdes.2014.10.019.
[19] Perić M, Nižetić S, Garašić I, Gubeljak N, Vuherer T, Tonković Z. Numerical calculation and experimental measurement of temperatures and welding residual stresses in a thick-walled T-joint structure. J Therm Anal Calorim 2020;141(1):313–22. http://dx.doi.org/10.1007/s10973-019-09231-3.
[20] Zhu J, Khurshid M, Barsoum Z. Accuracy of computational welding mechanics methods for estimation of angular distortion and residual stresses. Weld World 2019;63(5):1391–405. http://dx.doi.org/10.1007/s40194-019-00746-9.
[21] Perić M, Tonković Z, Rodić A, Surjak M, Garašić I, Boras I, Švaić S. Numerical analysis and experimental investigation of welding residual stresses and distortions in a T-joint fillet weld. Mater Des 2014;53:1052–63. http://dx.doi.org/10.1016/j.matdes.2013.08.011.
[22] Fu G, Lourenço MI, Duan M, Estefen SF. Influence of the welding sequence on residual stress and distortion of fillet welded structures. Mar Struct 2016;46:30–55. http://dx.doi.org/10.1016/j.marstruc.2015.12.001.
[23] Rikken M, Pijpers R, Slot H, Maljaars J. A combined experimental and numerical examination of welding residual stresses. J Mater Process Technol 2018;261:98–106. http://dx.doi.org/10.1016/j.jmatprotec.2018.06.004.
[24] Xin H, Veljkovic M. Residual stress effects on fatigue crack growth rate of mild steel S355 exposed to air and seawater environments. Mater Des 2020;193:108732. http://dx.doi.org/10.1016/j.matdes.2020.108732.
[25] Tankova T, da Silva LS, Balakrishnam M, Rodrigues D, Launert B, Pasternak H, Tun TY. Residual stresses in welded I section steel members. Eng Struct 2019;197:109398. http://dx.doi.org/10.1016/j.engstruct.2019.109398.
[26] Xing Y, Wang W, Al-azzani H. Assessment of thermal properties of various types of high-strength steels at elevated temperatures. Fire Saf J 2021;122:103348. http://dx.doi.org/10.1016/j.firesaf.2021.103348.
[27] Sun J, Hensel J, Klassen J, Nitschke-Pagel T, Dilger K. Solid-state phase transformation and strain hardening on the residual stresses in S355 steel weldments. J Mater Process Technol 2019;265:173–84. http://dx.doi.org/10.1016/j.jmatprotec.2018.10.018.
[28] Chiocca A, Frendo F, Aiello F, Bertini L. Influence of residual stresses on the fatigue life of welded joints. Numerical simulation and experimental tests. Int J Fatigue 2022;162:106901.
[29] Rosenthal D. Mathematical theory of heat distribution during welding and cutting. Weld J 1941;20:220–34.
[30] Rosenthal D. The theory of moving sources of heat and its application to metal treatments. Trans Am Soc Mech Eng 1946;68(8):849–65. http://dx.doi.org/10.1115/1.4018624.
[31] Rykalin N, Nikolaev A. Welding arc heat flow. IIW; 1970.
[32] Pavelic V. Experimental and computed temperature histories in gas tungsten arc welding of thin plates. Weld J Res Suppl 1969;48:296–305.
[33] Goldak J, Chakravarti A, Bibby M. A new finite element model for welding heat sources. Metall Trans B 1984;15(2):299–305. http://dx.doi.org/10.1007/BF02667333.
[34] EN C. 1011-1. In: Recommendations for welding of metallic materials, general guidance for arc welding.
[35] Van der Aa EM. Local cooling during welding: prediction and control of residual stresses and buckling distortion. 2007.
[36] Nguyen N, Ohta A, Matsuoka K, Suzuki N, Maeda Y. Analytical solutions for transient temperature of semi-infinite body subjected to 3-D moving heat sources. Weld J NY 1999;78:265–s.
[37] Xin H, Correia JA, Veljkovic M, Berto F, Manuel L. Residual stress effects on fatigue life prediction using hardness measurements for butt-welded joints made of high strength steels. Int J Fatigue 2021;147:106175. http://dx.doi.org/10.1016/j.ijfatigue.2021.106175.
[38] van den Berg N, Xin H, Veljkovic M. Effects of residual stresses on fatigue crack propagation of an orthotropic steel bridge deck. Mater Des 2021;198:109294. http://dx.doi.org/10.1016/j.matdes.2020.109294.
[39] Sattari-Far I, Farahani M. Effect of the weld groove shape and pass number on residual stresses in butt-welded pipes. Int J Press Vessels Pip 2009;86(11):723–31. http://dx.doi.org/10.1016/j.ijpvp.2009.07.007.
[40] LaRue J, Daniewicz S. Predicting the effect of residual stress on fatigue crack growth. Int J Fatigue 2007;29(3):508–15. http://dx.doi.org/10.1016/j.ijfatigue.2006.05.008.
[41] Walker K. The effect of stress ratio during crack propagation and fatigue for 2024-T3 and 7075-T6 aluminum. 1970, http://dx.doi.org/10.1520/STP32032S.
[42] Paris P, Erdogan F. A critical analysis of crack propagation laws. 1963, http://dx.doi.org/10.1115/1.3656900.
[43] BSI. Guide to methods for assessing the acceptability of flaws in metallic structures. Br Stand Inst 2015. BS 7910:2013+A1:2015.
[44] Dowling N, Calhoun C, Arcari A. Mean stress effects in stress-life fatigue and the Walker equation. Fatigue Fract Eng Mater Struct 2009;32(3):163–79. http://dx.doi.org/10.1111/j.1460-2695.2008.01322.x.
[45] Tang L, Ince A, Zheng J. Numerical simulation of residual stresses in welding and ultrasonic impact treatment process. In: Residual stress analysis on welded joints by means of numerical simulation and experiments. IntechOpen; 2018, http://dx.doi.org/10.5772/intechopen.72394.
[46] Ohta A, Sasaki E, Nihei M, Kosuge M, Kanao M, Inagaki M. Fatigue crack propagation rates and threshold stress intensity factors for welded joints of HT80 steel at several stress ratios. Int J Fatigue 1982;4(4):233–7. http://dx.doi.org/10.1016/0142-1123(82)90006-8.
[47] Beghini M, Bertini L, Vitale E. Fatigue crack growth in residual stress fields: experimental results and modelling. Fatigue Fract Eng Mater Struct 1994;17(12):1433–44. http://dx.doi.org/10.1111/j.1460-2695.1994.tb00786.x.
[48] Kang KJ, Song J, Earmme YY. Fatigue crack growth and closure through a tensile residual stress field under compressive applied loading. Fatigue Fract Eng Mater Struct 1989;12(5):363–76. http://dx.doi.org/10.1111/j.1460-2695.1989.tb00545.x.
[49] Bate S, Green D, Buttle D. A review of residual stress distributions in welded joints for the defect assessment of offshore structures. 1998.
[50] Bueckner H. Novel principle for the computation of stress intensity factors. Z Angew Math Mech 1970;50(9).
[51] Fett T, Munz D, Neumann J. Local stress intensity factors for surface cracks in plates under power-shaped stress distributions. Eng Fract Mech 1990;36(4):647–51. http://dx.doi.org/10.1016/0013-7944(90)90120-6.